Edinburgh Research Explorer

Mesoporous Ti0.5Cr0.5N for trace H2S detection with excellent long-term stability

Mesoporous $Ti_{0.5}Cr_{0.5}N$ for Trace H_2S Detection with Excellent Long-term Stability

Chaozhu Huang[a,b], Dongliang Liu[a], Dongting Wang[a], Haichuan Guo[a], Tiju Thomas[c], J. Paul Attfield[d],

Fengdong Qu[a,e,*], Shengping Ruan[e,*], Minghui Yang[a,b,*]

[a]*Ningbo Institute of Materials Technology and Engineering, Chinese Academy of Sciences, Ningbo*

315201, PR China.

[b]*Center of Materials Science and Optoelectronics Engineering, University of Chinese Academy of*

Sciences, Beijing 100049, China.

[c]*Department of Metallurgical and Materials Engineering, Indian Institute of Technology Madras*

Adyar, Chennai 600036, India.

[d]*Centre for Science at Extreme Conditions and School of Chemistry, University of Edinburgh, King's*

Buildings, Mayfield Road, Edinburgh, EH9 3JZ, United Kingdom.

[e]*State Key Laboratory on Integrated Optoelectronics, College of Electronic Science and Engineering,*

Jilin University, Changchun, 130012, China

Email:fqu@nimte.ac.cn (F. Qu),ruansp@jlu.edu.cn (S. Ruan) , myang@nimte.ac.cn(M. Yang)

Abstract:

Efficient, accurate and reliable detection and monitoring of H_2S is of significance in a wide range of areas: industrial production, medical diagnosis, environmental monitoring, and health screening. However the rapid corrosion of commercial platinum-on-carbon (Pt/C) sensing electrodes in the presence of H_2S presents a fundamental challenge for fuel cell gas sensors. Herein we report a solution to the issue through the design of a sensing electrode, which is based on Pt supported on mesoporous titanium chromium nitrides ($Pt/Ti_{0.5}Cr_{0.5}N$). Its desirable characteristics are due to its high electrochemical stability and strong metal-support interactions. The $Pt/Ti_{0.5}Cr_{0.5}N$-based sensors exhibit a much smaller attenuation (1.3%) in response to H_2S than Pt/C-sensor (42%), after 2 months sensing test. Furthermore, the $Pt/Ti_{0.5}Cr_{0.5}N$-based sensors exhibit negligible cross response to other interfering gases compared with hydrogen sulfide. Results of density functional theory calculation also verify the excellent long-term stability and selectivity of the gas sensor. Our work hence points to a new sensing electrode system that offers a combination of high performance and stability for fuel-cell gas sensors.

Keywords: Solid-solid separation method, $Ti_{0.5}Cr_{0.5}N$, Room-temperature, Fuel cell gas sensor, Hydrogen sulfide

1.Introduction

Hydrogen sulfide (H_2S), carbon monoxide (CO) and volatile organic compounds (VOCs) are among the common industrial exhaust gases which present serious health and ecological concerns.[1-4] H_2S is a dangerous neurotoxic gas which is colorless, inflammable, corrosive and has the odor of rotten eggs.[5] Studies have shown that exposure to 5 ppm (v) of H_2S can affect ophthalmic and respiratory health, while 100 ppm (v) causes irreversible damage to the central nervous system. On the other hand, more than 1000 ppm (v) can result in death within minutes.[6, 7] According to the recommendations of the Scientific Advisory Board on Toxic Air Pollutants (USA), the acceptable environmental levels of H_2S for humans should not exceed the range of 20-100 ppb (v).[8] It may be noted that endogenous H_2S is also one of the important gas markers in health screening and medical diagnosis.[9-11] In addition, H_2S as an impurity causes great harm to the service life and safety of energy generator system and increases heavy operating costs.[12, 13] The research shows that the content of H_2S in the operating atmosphere of solid oxide fuel cell (SOFC) and internal combustion engine (ICE) should not exceed 10ppm, or even reach the sub ppm level.[14, 15] However, detection of H_2S in an accurate and rapid manner in real time remains a practical challenge.

The difficulties with H_2S sensing has to do with the fact that there exist limitations associated with portability and cost of sensors. Especially for the detection of trace compounds, spectroscopy, chromatography and mass spectrometry often need to make a compromise in terms of cost or real-time detection.[16-18] Amperometric gas sensors that rely on direct conversion of current from electrode reaction to detectible species have attracted much attention. Their promise is due to their low power

3

55   consumption, low cost, small size, good linear response and fast response time.[19-21] Proton

56   exchange membrane (PEM) fuel cell type gas sensor, which uses Nafion N-115 membrane as the

57   constituent solid electrolyte works at room temperature without external voltage.[22] It is in fact one of

58   the most important amperometric gas sensors. Unfortunately, there are several obstacles to realize the

59   advantages of PEM fuel cell type sensors in sensing scenarios. The main challenge has been to find

60   more stable, sensitive and efficient electrode sensing materials.[23]

61   Efforts have been directed towards overcoming challenges. Bimetallic catalysts with synergistic effect,

62   such as Pt-Ru,[24] Pt-Sn[25] and Pt-alloy[26] have been utilized to replace Pt/C (the most commonly

63   used catalyst for PEM fuel cells). Although these catalysts exhibit improved selectivity and sensitivity,

64   porous carbon inherently corrodes easily into carbon oxides under electrochemical oxidation

65   conditions and hence lacks long-term stability.[27] This in turn leads to desorption of Pt from the

66   support and further agglomeration, thus rendering the gas sensor ineffective. Other studies have shown

67   that carbon support modification is another strategy to improve the stability of the catalytic layer. For

68   example, Chen et al. have used Pt-S-C to enhance the interaction between Pt and C.[28] However,

69   modification with S doping makes the binding between H_2S and Pt relatively weak, thus rendering this

70   anode material unfavorable for H_2S gas sensing. Therefore, it is necessary to develop a sensing

71   material with outstanding stability and sensitivity.

72   Transition metal nitrides (TMNs) have been considered as promising catalyst support in PEM fuel

73   cells due to their high (metallic) electrical conductivity, high catalytic performance and thermal and

74 electrochemical stabilities.[29-32] For example, we previously reported that mesoporous TMNs

75 (TiN[33] and WN[22]) not only act as support for Pt, but also show enhanced sensing performance

76 compared with carbon black. In addition, by tuning the composition and/or surface chemistry,

77 enhanced tolerance to corrosion in highly acidic environment can be achieved.[34] We have thus

78 hypothesized that mesoporous ternary TMNs can act as a support for Pt, which integrates the

79 advantages of the binary nitrides. There is a strong interactions between ternary TMNs and Pt, which

80 enhances their interaction and leads to a change of the electronic structure of Pt atom.[35-37] Such

81 change may lead to predictable variations in the adsorption energy, electron transfer pathway and

82 reaction activation energy of different gases by the catalyst-support, thereby improving the stability,

83 selectivity and sensitivity of gas sensors.

84 Herein, we report an effort to improve the stability of a fuel cell type gas sensor. This approach uses

85 mesoporous $Ti_{0.5}Cr_{0.5}N$ as a replacement for carbon black as the support for Pt. We show that this

86 results in significant improvement in gas sensing performance of H_2S. $Pt/Ti_{0.5}Cr_{0.5}N$ sensor. In fact

87 the sensor is shown to operate in demanding atmospheres without any significant of deactivation,

88 even after 2 months. Simultaneously, the sensitivity as well as selectivity is improved, and the sensor

89 limit of detection (LoD) is significantly enhanced (10 ppb (v)).

90 **2. Experimental**

91 **2.1. Materials**

92 All chemicals are purchased from commercial grade and can be used without further purification. Zinc

93 oxide (ZnO, 99%) and isopropanol (anhydrous, 99.5%) are purchased from Macklin. Titanium oxide

94 (TiO$_2$, 99%), chromium oxide (Cr$_2$O$_3$, 99%), chloroplatinic acid hexahydrate (H$_2$PtCl$_6$·6H$_2$O, 99.9%)

95 and ethylene glycol (anhydrous, 99%) are obtained from Aladdin, Damao Chemical Reagent Factory,

96 Adamas and Sinopharm, respectively. The commercial platinum-on-carbon black (Pt/C, 20 wt% Pt) is

97 purchased from Johnson Matthey.

98 **2.2. Preparation of mesoporous Ti$_{0.5}$Cr$_{0.5}$N**

99 Mesoporous Ti$_{0.5}$Cr$_{0.5}$N are synthesized by a solid-solid phase separation method from a Zn containing

100 metal oxides. Firstly, the fully mixed ZnO, Cr$_2$O$_3$, and TiO$_2$ powders are heated at 700 °C and 1000 °C

101 for 8 h and 24 h, respectively, to prepare oxide precursors. Then, approximately 0.5 g of the precursor

102 is placed into a silica boat in a tubular furnace with ammonia as the flowing gas (flow rate of 200

103 cm^3/min), and heat treated at 800 °C for 12 h. After the ammonolysis reaction is completed, the system

104 is kept in ammonia atmosphere until the tube furnace cools to room temperature. Before removing the

105 sample from the tubular furnace, the tube is placed in the lab for 24 h with only one end slightly open to

106 form an extremely thin oxide on the surface of Ti$_{0.5}$Cr$_{0.5}$N. (TiN, Ti$_{0.25}$Cr$_{0.75}$N, Ti$_{0.75}$Cr$_{0.25}$N and CrN

107 are synthesized by a similar method).

108 **2.3. Preparation of Pt/Ti$_{0.5}$Cr$_{0.5}$N**

109 Platinum nanoparticles are deposited by ethylene glycol reduction method. Firstly, the 50 mg

110 Ti$_{0.5}$Cr$_{0.5}$N is dispersed in the Teflon-lined containing 50 ml ethylene glycol, and homogenized

111 alternately by stirring and ultrasonic. Then, 1.3 mL of 50 mM H$_2$PtCl$_6$ solution is added to the

112 suspension and sonicated in an ice water bath for 30 minutes. Next, the Teflon-lined is placed in a

113 stainless steel autoclave and heated to 140 °C for 3 h. After that, the product is filtered and the

114 precipitate is washed alternately with deionized water and alcohol three times to remove ethylene

115 glycol. Finally, the product is left in a vacuum box at 60 °C overnight to obtained $Pt/Ti_{0.5}Cr_{0.5}N$ powers.

116 According to the ICP results, the actual Pt loading of $Pt/Ti_{0.5}Cr_{0.5}N$ and Pt/C(JM) are found to be

117 17.2wt% and 17.2wt%, respectively.

118 **2.4. Sensor fabrication**

119 The fuel cell type gas sensor is made of Membrane electrode assembly（MEA), two pieces of stainless

120 steel electrode with good electrical conductivity and a water container. MEA is the core component of

121 the sensor, and its preparation method is as follows: firstly, 5 mg $Pt/Ti_{0.5}Cr_{0.5}N$ powder and 40 μl of

122 5wt% are solubilized Nafion (DUPONT, USA.). It is then added to 800 μL of solution of isopropanol

123 and deionized water (volume ration = 1:1), followed by ultrasonic treatment to form catalyst ink.

124 Next, the ink is loaded to the surface of carbon paper (Shanghai, Hesen Co., Ltd) using air spraying

125 under 90 °C. And then two pieces of carbon paper are combined with NafionN-115 membrane

126 (DUPONT, USA.), two PTFE membrane are used as protective layer, and hot press is performed at

127 90 °C and at 1 MPa for 120 s. After that, the PTFE membranes are teared off to obtain MEA. The

128 pretreatment of Nafion membrane is consistent with the method that we used before.[22]

129 The carbon paper facilitates the uniform loading of the catalyst layer on the working electrode and the

130 counter electrode. The MEA is cut to match the size of the stainless steel electrode (the diameter is 1.0

131 cm), and it is combined with the stainless steel electrode using a hot melt glue to form a small fuel cell.

132 Then, the cathode of the cell is sealed with a water container, which contains an absorbent cotton

133 soaked by deionized water. The working electrode is exposed to external target gas while the counter

134 electrode is sealed in an isolation chamber filled with wet air when the device is in operation.

2.5. Computational methodology

136 Density functional theory (DFT) calculations are performed with the Dmol3 package code in Material

137 Studio 8.0. the double numerical plus polarization (DNP) basis set and the generalized-gradient

138 approximation (GGA) with the Perdew-Burke-Emzerhof (PBE) are employed to obtain all the results

139 reported below.[38, 39] In order to avoid the interaction between adjacent cells, a vacuum slab of 15 Å

140 width is used. The core treatment is set as Effective Core Potential to manage the interaction between

141 the nucleus and valence electrons. The Brillouin zone k-point sampling is performed in $2\times2\times1$

142 Monkhorst-Pack mesh. The energy tolerance accuracy, maximum force, and displacement are set as

143 10^{-5} Ha, 2×10^{-2} Ha/Å, 3.7 Å and 5×10^{-2} Å, respectively. For static electronic structure calculations,

144 self-consistent loop energy of 10^{-5} Ha and smearing of 0.005 Ha aare employed to ensure the accurate

145 results of total energy.[40] The adsorption energy (E_{ads}) of each system is calculated by the following

146 equation (1):

147 $$E_{ads} = E_{gas} + E_{catalystr} - E_{gas/catalyst} \quad (1)$$

148 In the formulation, E_{gas}, $E_{catalyst}$ and $E_{gas/catalyst}$ refer to the total energies of the gas molecule, the catalyst,

149 and the gas adsorption system, respectively. And the formation energy (E_{for}) between Pt and support is

150 calculated by the following equation (2):

151 $$E_{for} = E_{Pt/support} - (E_{Pt} + E_{support}) \quad (2)$$

152 $E_{Pt/support}$, E_{Pt} and $E_{support}$ are the total energies of the support combined with Pt, Pt and support,

153 respectively.

2.6. Characterization

155 The phase information and lattice parameters of prepared catalyst powders are characterized using

156 X-ray diffraction (XRD, Rigaku MiniFlex 600 powder X-ray diffractometer with Cu K_α radiation at λ

157 = 1.5418 Å, scanning speed: 0.1° min^{-1}, 2θ range of 10-85°). To observe the surface morphology of

158 the materials, scanning electron microscope (SEM) is used with Verios G4 UC (USA). The HRTEM

159 (high-resolution transmission electron microscopy) images and the HAADF-STEM (high-angle

160 annular dark field scanning transmission electron microscope) images are performed through Talos

161 F200x (America). X-ray photoelectron spectroscopy (XPS) is performed using AXIS SUPRA (UK).

162 The binding energies of $Pt/Ti_{0.5}Cr_{0.5}N$ and Pt/C surface are calibrated by C 1s peak (284.8 eV). In order

163 to determine the actual content of platinum in $Pt/Ti_{0.5}Cr_{0.5}N$ and Pt/C, inductively coupled plasma

164 emission spectrometer (ICP, SPECTROARCOS II, Germany) is used. The BET results of $Ti_{0.5}Cr_{0.5}N$

165 and Pt/C are obtained by an automatic specific surface area and microporous pore analyzer

166 (ASAP2020HD88, America). The gas sensing performance is tested by a multichannel potentiostat

167 (CHI1030C, Shanghai Chenhua Instrument Co., Ltd) using the amperometric i-t curve at zero potential

168 applied.

3. Results and discussion

3.1. Structural and morphological characteristics

171 Titanium chromium nitride crystalline powders are prepared using solid-solid phase separation of

172 zinc containing metal oxides. (Fig. 1a-b) The precursor oxide ($Zn_5Ti_2Cr_2O_{12}$) formed by melting is

173   ammonolyzed at 800 °C. Zn ions are therefore evaporated away, and nitrogen anions replace oxygen

174   anions to form mesoporous nitrides. $Pt/Ti_{0.5}Cr_{0.5}N$ sensing catalyst is prepared by reducing

175   chloroplatinic acid ($H_2PtCl_6 \cdot 6H_2O$) with ethylene glycol to achieve uniform distribution of Pt NPs on

176   the nitride surface. (Fig. 1c). As shown in Fig. 1d-f, the catalyst ink is evenly dispersed on the gas

177   diffusion layer by air spraying, and then the fuel cell type gas sensor is assembled using a series of

178   processes (see experimental section for details). The fuel cell type gas sensor consist of MEA,

179   electrode and cathode sealing chamber.

180   Formation of crystalline $Ti_{0.5}Cr_{0.5}N$ and $Pt/Ti_{0.5}Cr_{0.5}N$ are confirmed using Rietveld refinement using

181   powder x-ray diffraction (XRD) data (Fig. 2a). There is no appearance of peaks associated with any

182   other phases, thus indicating lack of any impurities. In addition, TMNs with different Ti and Cr ratios

183   are successfully synthesized (Fig. S1). The surface chemical properties are further confirmed by using

184   X-ray photoelectron spectroscopy (XPS) (Fig. S2 and S3). The corresponding high-resolution Pt 4f

185   spectra are shown in Fig. 2b. The comparison of the relative areas of their integral intensities shows

186   that more Pt (0) is observed in $Pt/Ti_{0.5}Cr_{0.5}N$ catalyst than Pt/C catalyst. This contributes to increased

187   catalytic activity of the sensor.[41]

188   For Pt (0) peak, the Pt 4f binding energy of $Pt/Ti_{0.5}Cr_{0.5}N$ has an obvious negative shift of about 0.5

189   eV compared with that of Pt/C catalyst. This confirms the strong interaction between Pt and

190    $Ti_{0.5}Cr_{0.5}N$ support. The negative shift of binding energy indicates that Pt nanoparticles can draw

191   electrons from $Ti_{0.5}Cr_{0.5}N$ support, leading to changes in the surface electronic structure of Pt.[41, 42]

192   This provides the appropriate charge transfer for enhancement of the gas sensing response.

193   From the scanning electron microscope (SEM) and transmission electron microscope (TEM) images,

194   it is clear that a mesoporous $Ti_{0.5}Cr_{0.5}N$ has formed and size of pores in the range of 10-30 nm (Fig.2

195   c). Furthermore, it is evident that Pt NPs of 1-3 nm are uniformly deposited on the support material

196   (Fig. 2d). As is seen from high resolution TEM (HRTEM) image in Fig. 2e, lattice fringes of

197     $Ti_{0.5}Cr_{0.5}N$ and Pt are detected. These fringes correspond to the $Ti_{0.5}Cr_{0.5}N$ (200) plane (with

198   interplanar spacing = 2.13 Å). Likewise, the 2.25 Å interplanar spacing correspond to the Pt (111)

199   plane. In addition, the high-angle annular dark-field scanning TEM (HAADF-STEM) image and the

200   corresponding EDX mapping images are given in Fig. 2f. This proves the presence and homogenous

201   distribution of Ti, Cr, N and Pt elements.

202   The abundant and interconnected pores indicate that $Pt/Ti_{0.5}Cr_{0.5}N$, owing to its porous nature, has

203   surfaces that are highly gas-accessible. This is supported using Brunauer–Emmett–Teller (BET)

204   analysis (Fig. S4). The nitrogen adsorption and desorption isotherms of the $Ti_{0.5}Cr_{0.5}N$ show type IV

205   isotherms with H3 hysteresis loops. The Barrett–Joyner–Halenda surface area is found to be 36.6

206   m^2g^{-1}. The pore size distribution (adsorption average pore width is 23.9 nm) determined suggests the

207   presence of mesopores formed by the sublimation of Zn. The results of the SEM, TEM, and BET

208   analyses indicate that mesoporous $Ti_{0.5}Cr_{0.5}N$ with high surface area-to-volume ratios as well as highly

209   gas-accessible structures are advantageous as Pt supports.

210   **3.2. Gas sensing properties**

211   The chosen composition is optimal as $Ti_{0.5}Cr_{0.5}N$ exhibits the highest response to 100 ppm (v) H_2S (Fig.

212   3a and Fig. S5). Pt/Ti$_{0.5}$Cr$_{0.5}$N and Pt/C sensors exhibit similar response and recovery characteristics.

213   The response time and recovery time to 100 ppm (v) H$_2$S are 23 / 23 s and 24 / 25 s, respectively (Fig.

214   S6). The dynamic sensing responses (defined as I_G -I_0, ΔI) of Pt/Ti$_{0.5}$Cr$_{0.5}$N and Pt/C sensors toward

215   H$_2$S with various concentration (from 10 ppb (v) to 50 ppm (v)) are measured (Fig. 3b). Compared

216   with Pt/C sensor, Pt/Ti$_{0.5}$Cr$_{0.5}$N sensor exhibits better response toward H$_2$S (by more than 200%). In

217   addition, the standard deviation of the Pt/Ti$_{0.5}$Cr$_{0.5}$N sensor at different concentrations is within 4%

218   (ppm level) or 10% (ppb level) of its response current (Fig. S7).

219   Although both Pt/Ti$_{0.5}$Cr$_{0.5}$N and Pt/C sensors exhibit a positive linear response toward H$_2$S in the

220   range 10 ppb (v) - 50 ppm (v) (Fig. 3c), Pt/Ti$_{0.5}$Cr$_{0.5}$N sensor has a higher sensitivity (0.629 µA/ppm

221   (v)) than that of Pt/C sensor (0.252 µA/ppm (v)). Most importantly, Pt/Ti$_{0.5}$Cr$_{0.5}$N performs well at

222   10-500 ppb (v) levels (inset of Fig. 3b), with LoD as low as 10 ppb (v). This is to be contrasted with

223   Pt/C's lack of recognizable current signals at 50 ppb (v). In addition, the baseline current of the sensor

224   operating in air for 30 min is collected (Fig. 3d). Based on the root mean square deviation (RMSD)

225   method, the detection limits of Pt/Ti$_{0.5}$Cr$_{0.5}$N and Pt/C sensors are 0.46 ppb (v) and 12.30 ppb (v),

226   respectively. Lower current fluctuations contribute to the recognition of the sensor response signal. At

227   the same time, the strong interaction between support and metal can promote the catalytic oxidation of

228   adsorbed gases on the catalyst surface by transferring electrons from Ti$_{0.5}$Cr$_{0.5}$N to Pt NPs. Therefore,

229   the Ti$_{0.5}$Cr$_{0.5}$N-based sensor exhibits a lower limit of detection.

230   Selectivity is another essential parameter to evaluate the performance of gas sensors. Comprehensive

231 evaluation of the selectivity of different components, $Ti_{0.5}Cr_{0.5}N$ demonstrates the best selectivity for

232 H_2S among the sensors studied (Fig. S8). The response of $Pt/Ti_{0.5}Cr_{0.5}N$ and Pt/C sensors toward

233 different gases, including carbonic oxide (CO), hydrogen (H_2), methanol (CH_3OH)，ethanol

234 (C_2H_5OH), formaldehyde (HCHO) and hydrogen sulphide (H_2S) at the same concentration (100 ppm

235 (v)) is tested (Fig. 3e). Pt/C sensor show a slight selectivity for H_2S over the other gases tested.

236 However, CO and other volatile organic compounds (VOCs, such as ethanol, methanol,

237 formaldehyde, etc.) causes strong cross sensitivity, which is not conducive to the detection of

238 specific gases. However, the $Pt/Ti_{0.5}Cr_{0.5}N$ sensor displays high response to H_2S, with negligible

239 response to other interfering gases. This implies excellent selectivity to H_2S.

240 Fig. 3f clearly shows that $Pt/Ti_{0.5}Cr_{0.5}N$ sensor exhibits improved selectivity ($\Delta I_{H2S}/\Delta I_{other\ gas}$) toward

241 H_2S when compared with that of Pt/C sensor. For CO, H_2 and hydroxyl-containing VOC gases, the

242 response of $Pt/Ti_{0.5}Cr_{0.5}N$ sensor is significantly reduced, which may be due to the change in the

243 gases adsorption at the three-phase reaction interface. Besides, the electronic structure of Pt NPs is

244 affected by the $Ti_{0.5}Cr_{0.5}N$ support, leading to the different electrochemical activity for various gases.

245 This accounts for improved selectivity.[41, 43, 44]

246 The response variation and attenuation during long-term operation remain an unsolved issue that

247 reduces sensor accuracy and causes more complications in sensor calibrations.[45-47] The cyclic and

248 long-term stability of $Pt/Ti_{0.5}Cr_{0.5}N$ sensor are presented. Fig. 4a shows a 7-cycle dynamic sensing

249 response of $Pt/Ti_{0.5}Cr_{0.5}N$ sensor to 100 ppm (v) H_2S. A fluctuation of ~4% can be calculated,

250   thereby indicating excellent cyclic stability. In particular, after two months of exposure to operating

251   conditions, the Pt/Ti$_{0.5}$Cr$_{0.5}$N sensor retained its response (1.3% attenuation), while the Pt/C sensor

252   gets significantly deactivated (40%) (Fig. 4b and 4c). Hence excellent sensing performance is clearly

253   retained in the long term.

254   The above clearly demonstrates that the ternary nitride Ti$_{0.5}$Cr$_{0.5}$N displays excellent long-term

255   stability, superior to the carbon support. In addition, Pt/Ti$_{0.5}$Cr$_{0.5}$N also offers the lowest sensitivity

256   drift and limit of detection compared with selected fuel cell type sensors and 2-electrode commercial

257   electrochemical H$_2$S sensors (Fig. 4d). Based on the summary of gas sensing devices for H$_2$S sensing

258   characteristics reported recently (Table S1), we note that the Pt/Ti$_{0.5}$Cr$_{0.5}$N sensor working at room

259   temperature exhibits lower LoD, higher sensitivity and better stability, and hence has the potential to

260   be applied to a variety of H$_2$S detection requirements.

261   To explore the reason for the difference in stability of Pt/Ti$_{0.5}$Cr$_{0.5}$N and Pt/C sensors, the TEM

262   images of the electrode catalysts of the two sensors at 100 ppm (v) H$_2$S and at different aging states

263   are characterized (Fig. S9). Fig. S9a and S9b shows TEM images of the Pt/Ti$_{0.5}$Cr$_{0.5}$N sensor before

264   gas sensing and after continuous H$_2$S sensing for 60 days, respectively. Compared with the newly

265   prepared electrode catalyst, the morphology and structure of the material after 60 days of H$_2$S

266   sensing did not collapse, therefore showing excellent chemical stability. A slight grain growth of Pt

267   nanoparticles is observed, which may be the reason for the slight drift of response time of sensor.

268   However, in case of the Pt/C sensor, the carbon black support material is completely oxidized after

269 60 days of H$_2$S detection, which is concomitant with severe agglomeration and crystal growth of Pt

270 NPs compared to before gas detection (Fig. S9d and S9e).

271 As illustrated in Fig. S9c and S9f, we calculate the Pt NPs size distribution of Pt/Ti$_{0.5}$Cr$_{0.5}$N and Pt/C

272 sensors at different aging states (fresh and two months later). It is clearly evident that the

273 agglomeration degree of Pt NPs in the Pt/C sensor is much more serious than that of the

274 Pt/Ti$_{0.5}$Cr$_{0.5}$N sensor. For the catalyst before the gas test, the Pt nanoparticles of the two sensors are

275 in fact distributed in the range of 1-3, 1-5 nm, respectively. After 60 days of testing, the size of most

276 of the Pt NPs (more than 90%) on the Ti$_{0.5}$Cr$_{0.5}$N is still within 1–3.5 nm. However, the number of Pt

277 NPs on the carbon black support is significantly reduced (more than 50%). This may be caused by

278 desorption or agglomeration of Pt NPs; furthermore an increase in size (1-19 nm) also observed.

279 **3.3. DFT calculations**

280 DFT calculations are performed to unravel the role that mesoporous titanium chromium nitrides play

281 in the H$_2$S detection. Gas adsorption is an important step for the sensitive electrode to catalyze the

282 target gas. Higher adsorption energy is conducive to the catalysis of gas on the electrode surface and

283 improve the detection ability of the target gas. The appropriate support can affect the gas adsorption of

284 the catalyst at the three-phase interface.[48] On the surface of Pt/Ti$_{0.5}$Cr$_{0.5}$N, the adsorption energies of

285 various analyte gases on the catalyst are presented in Fig. 5a. The adsorption energy of H$_2$S is much

286 higher than that of other gases, which may be one of the reasons why the sensor has good selectivity for

287 H$_2$S. The strong interaction between support and metal is also one of the decisive reasons for the

288 long-term stability of the catalyst. The low formation energy indicates that the gas sensing material is

289 more stable, which is conducive to improve the stability of the sensor. Fig. 5b displays the formation

290 energy of Pt combined with support, and the results demonstrate that the formation energy of

291 $Pt/Ti_{0.5}Cr_{0.5}N$ is lower (less than 0 eV). This is also a reason why the $Pt/Ti_{0.5}Cr_{0.5}N$ sensor exhibits

292 long-term stability far exceeding that of the Pt/C sensor.

293 In addition, we have also explored the reaction process of H_2S (Fig. S10). The oxidation of H_2S can be

294 divided into two steps: I) $H_2S \rightarrow HS+H$ and II) $HS \rightarrow S+H$.[49-51] We construct the optimized

295 structures of reactants, intermediates and products, and calculate the relative potential energy and

296 reaction energies between the corresponding key steps. The results indicate that second step requires a

297 larger activation energy (~3.62 eV), which is the rate control step. Exploring the decomposition steps

298 and reaction kinetics of hydrogen sulfide is helpful to explain the working principle of the sensor and

299 may be conducive to the design of new and efficient hydrogen sulfide sensing materials.

300 **3.4. Relative humidity**

301 In addition, relative humidity (RH) is another non-negligible factor that may affect the gas-sensing

302 performance of electrochemical sensors. Fig. 6 exhibits the baseline current and transient response of

303 the sensor at different relative humidity (11%, 33%, 55%, 75% and 95% RH). The baseline current is

304 nA level at different relative humidity and the difference is very small (less than 0.1 μA), current

305 fluctuation also shows acceptable results (Fig. 6a). This is conducive to the stable operation of the

306 sensor in the alternating dry and humid air environment. To explore the effect of gas humidity on the

307 sensing performance of the sensor, Fig. 6b exhibits the transient response of 100 ppm H_2S with

308   different humidity. It can be seen that the drift percentage of the response signal of the sensor is less

309   than 5%, which indicates that the influence of humidity on the sensing performance of the sensor is

310   very slight. This may be due to the sensor is equipped with a cathode sealed chamber, and high

311   humidity gas can quickly and effectively infiltrate MEA. Therefore, the gas humidity of the external

312   environment has little effect on the performance of the sensor. However, if the sensor needs to

313   operate in a low humidity atmosphere for a long time, it is necessary to inject water into the cathode

314   chamber regularly to maintain the conditions for efficient operation of MEA.

315   **4. Conclusion**

316   In conclusion, it is demonstrated that $Ti_{0.5}Cr_{0.5}N$ can be used as a support of fuel cell type sensor with

317   high efficiency, selectivity and stability. Hence the device reported has the potential to offer long-term,

318   drift-resistant H_2S sensing. It provides unique H_2S detection capability (ppb (v) level), with excellent

319   linear response in the concentration range of 0.01-50 ppm (v). Its sensitivity (0.629 μA/ppm) is more

320   than twice that of commercial Pt/C (0.252 μA/ppm). Importantly, we demonstrate that the

321    $Pt/Ti_{0.5}Cr_{0.5}N$ sensor has excellent cycle repeatability and long-term stability owing both to the stable

322   morphology and structure of the catalyst. $Pt/Ti_{0.5}Cr_{0.5}N$ maintained its response (1.3% attenuation)

323   even after the sensor is operated at 100 ppm (v) H_2S for two months continuously, while Pt/C shows

324   significant deactivated (40%). In addition, the results of gas sensing and DFT calculations reveal a

325   distinctive and selective sensitivity of the $Pt/Ti_{0.5}Cr_{0.5}N$ towards H_2S, which provides prospect for

326   furthering state of the art multifunctional sensors.

327   **Acknowledgments**

335

336 **References**

337 [1] X. Zheng, G. Zhang, Z. Yao, Y. Zheng, L. Shen, F. Liu, Y. Cao, S. Liang, Y. Xiao, L. Jiang,
338 Engineering of crystal phase over porous MnO_2 with 3D morphology for highly efficient elimination
339 of H_2S, J. Hazard. Mater. 411 (2021) 125180. https://doi.org/10.1016/j.jhazmat.2021.125180.

340 [2] X. Qiao, Y. Xu, K. Yang, J. Ma, C. Li, H. Wang, L. Jia, Mo doped $BiVO_4$ gas sensor with high
341 sensitivity and selectivity towards H_2S, Chem. Eng. J. 395 (2020).
342 https://doi.org/10.1016/j.cej.2020.125144.

343 [3] I. Boehme, U. Weimar, N. Barsan, Unraveling the Surface Chemistry of CO Sensing with In_2O_3
344 Based Gas Sensors, Sens. Actuators B Chem. 326 (2021). https://doi.org/10.1016/j.snb.2020.129004.

345 [4] D. Kuang, L. Wang, X. Guo, Y. She, B. Du, C. Liang, W. Qu, X. Sun, Z. Wu, W. Hu, Y. He, Facile
346 hydrothermal synthesis of $Ti_3C_2T_x$-TiO_2 nanocomposites for gaseous volatile organic compounds
347 detection at room temperature, J. Hazard. Mater. 416 (2021).
348 https://doi.org/10.1016/j.jhazmat.2021.126171.

349 [5] V. Kumar, S.M. Majhi, K.-H. Kim, H.W. Kim, E.E. Kwon, Advances in In_2O_3-based materials for
350 the development of hydrogen sulfide sensors, Chem. Eng. J. 404 (2021).
351 https://doi.org/10.1016/j.cej.2020.126472.

352 [6] L. Liu, Y. Wang, Y. Dai, G. Li, S. Wang, T. Li, T. Zhang, S. Qin, In Situ Growth of $NiO@SnO_2$
353 Hierarchical Nanostructures for High Performance H_2S Sensing, ACS Appl. Mater. Interfaces 11(47)
354 (2019) 44829-44836. https://doi.org/10.1021/acsami.9b13001.

355 [7] O. Yassine, O. Shekhah, A.H. Assen, Y. Belmabkhout, K.N. Salama, M. Eddaoudi, H_2S Sensors:
356 Fumarate-Based fcu-MOF Thin Film Grown on a Capacitive Interdigitated Electrode, Angew. Chem.
357 Int. Ed. 55(51) (2016) 15879-15883. https://doi.org/10.1002/anie.201608780.

358 [8] K. Tian, X.X. Wang, Z.Y. Yu, H.Y. Li, X. Guo, Hierarchical and Hollow Fe_2O_3 Nanoboxes
359 Derived from Metal-Organic Frameworks with Excellent Sensitivity to H_2S, ACS Appl. Mater.
360 Interfaces 9(35) (2017) 29669-29676. https://doi.org/10.1021/acsami.7b07069.

361 [9] W. Chen, D. Ni, Z.T. Rosenkrans, T. Cao, W. Cai, Smart H_2S-Triggered/Therapeutic System
362 (SHTS)-Based Nanomedicine, Adv. Sci. (Weinh) 6(22) (2019) 1901724.
363 https://doi.org/10.1002/advs.201901724.

364 [10] L. Sui, T. Yu, D. Zhao, X. Cheng, X. Zhang, P. Wang, Y. Xu, S. Gao, H. Zhao, Y. Gao, L. Huo, In
365 situ deposited hierarchical CuO/NiO nanowall arrays film sensor with enhanced gas sensing
366 performance to H_2S, J. Hazard. Mater. 385 (2020) 121570.
367 https://doi.org/10.1016/j.jhazmat.2019.121570.

368 [11] X. Xing, Z. Zhu, D. Feng, L. Du, D. Yang, The "screening behavior" of lithium: Boosting H_2S
369 selectivity of WO_3 nanofibers, J. Hazard. Mater. 416 (2021).
370 https://doi.org/10.1016/j.jhazmat.2021.125964.

371 [12] H. Wasajja, R.E.F. Lindeboom, J.B. van Lier, P.V. Aravind, Techno-economic review of biogas
372 cleaning technologies for small scale off-grid solid oxide fuel cell applications, Fuel Process. Technol.
373 197 (2020). https://doi.org/10.1016/j.fuproc.2019.106215.

374 [13] A. Baldinelli, L. Barelli, G. Bidini, G. Cinti, Micro-cogeneration based on solid oxide fuel cells:
375 Market opportunities in the agriculture/livestock sector, Int. J. Hydrog. Energy 46(16) (2021)

376 10036-10048. https://doi.org/10.1016/j.ijhydene.2020.04.226.

377 [14] A. Lanzini, D. Ferrero, D. Papurello, M. Santarelli, Reporting Degradation from Different Fuel
378 Contaminants in Ni-anode SOFCs, Fuel Cells 17(4) (2017) 423-433.
379 https://doi.org/10.1002/fuce.201600184.

380 [15] D. Papurello, L. Tognana, A. Lanzini, F. Smeacetto, M. Santarelli, I. Belcari, S. Silvestri, F.
381 Biasioli, Proton transfer reaction mass spectrometry technique for the monitoring of volatile sulfur
382 compounds in a fuel cell quality clean-up system, Fuel Process. Technol. 130 (2015) 136-146.
383 https://doi.org/10.1016/j.fuproc.2014.09.041.

384 [16] D. Papurello, Direct injection mass spectrometry technique for the odorant losses at ppb(v) level
385 from nalophan™ sampling bags, Int. J. Mass. Spectrom. 436 (2019) 137-146.
386 https://doi.org/10.1016/j.ijms.2018.12.008.

387 [17] D.W. You, Y.S. Seon, Y. Jang, J. Bang, J.S. Oh, K.W. Jung, A portable gas chromatograph for
388 real-time monitoring of aromatic volatile organic compounds in air samples, J. Chromatogr. A 1625
389 (2020) 461267. https://doi.org/10.1016/j.chroma.2020.461267.

390 [18] Y.-F. Zhao, J. Gao, Y.-J. Cai, J.-J. Wang, J. Pan, Real-time tracing VOCs, O_3 and PM2.5 emission
391 sources with vehicle-mounted proton transfer reaction mass spectrometry combined differential
392 absorption lidar, Atmospheric Pollut. Res. 12(3) (2021) 146-153.
393 https://doi.org/10.1016/j.apr.2021.01.008.

394 [19] Y. Gao, L. Yu, J.C. Yeo, C.T. Lim, Flexible Hybrid Sensors for Health Monitoring: Materials and
395 Mechanisms to Render Wearability, Adv. Mater. 32(15) (2020) e1902133.
396 https://doi.org/10.1002/adma.201902133.

397 [20] Z. Li, R. Liu, C. Tang, Z. Wang, X. Chen, Y. Jiang, C. Wang, Y. Yuan, W. Wang, D. Wang, S.
398 Chen, X. Zhang, Q. Zhang, J. Jiang, Cobalt Nanoparticles and Atomic Sites in Nitrogen-Doped Carbon
399 Frameworks for Highly Sensitive Sensing of Hydrogen Peroxide, Small 16(15) (2020) e1902860.
400 https://doi.org/10.1002/smll.201902860.

401 [21] J.R. Stetter, J. Li, Amperometric gas sensors - A review, Chem. Rev. 108(2) (2008) 352-366.
402 https://doi.org/10.1021/cr0681039.

403 [22] D. Meng, S. Zhang, T. Thomas, C. Huang, J. Zhao, R. Zhao, Y. Shi, F. Qu, M. Yang, Pt/WN based
404 fuel cell type methanol sensor, Sens. Actuators B Chem. 307 (2020).
405 https://doi.org/10.1016/j.snb.2020.127686.

406 [23] B.P. Vinayan, R. Nagar, N. Rajalakshmi, S. Ramaprabhu, Novel Platinum-Cobalt Alloy
407 Nanoparticles Dispersed on Nitrogen-Doped Graphene as a Cathode Electrocatalyst for PEMFC
408 Applications, Adv. Funct. Mater. 22(16) (2012) 3519-3526. https://doi.org/10.1002/adfm.201102544.

409 [24] X. Yang, Y. Zhang, X. Hao, Y. Song, X. Liang, F. Liu, F. Liu, P. Sun, Y. Gao, X. Yan, G. Lu,
410 Nafion-based amperometric H_2S sensor using Pt-Rh/C sensing electrode, Sens. Actuators B Chem.
411 273 (2018) 635-641. https://doi.org/10.1016/j.snb.2018.06.087.

412 [25] X. Yang, W. Li, Y. Zhang, T. Liu, X. Hao, R. Zhou, X. Liang, F. Liu, F. Liu, Y. Gao, X. Yan, G.
413 Lu, Fuel cell type H_2S sensor utilizing Pt-Sn-C/Nafion sensing electrode, Sens. Actuators B Chem.
414 299 (2019). https://doi.org/10.1016/j.snb.2019.126972.

415 [26] M. Zamanzad Ghavidel, M.R. Rahman, E.B. Easton, Fuel cell-based breath alcohol sensors

utilizing Pt-alloy electrocatalysts, Sens. Actuators B Chem. 273 (2018) 574-584. https://doi.org/10.1016/j.snb.2018.06.078.

[27] A. Zadick, L. Dubau, N. Sergent, G. Berthomé, M. Chatenet, Huge Instability of Pt/C Catalysts in Alkaline Medium, ACS Catal. 5(8) (2015) 4819-4824. https://doi.org/10.1021/acscatal.5b01037.

[28] D. Higgins, M.A. Hoque, M.H. Seo, R. Wang, F. Hassan, J.-Y. Choi, M. Pritzker, A. Yu, J. Zhang, Z. Chen, Development and Simulation of Sulfur-doped Graphene Supported Platinum with Exemplary Stability and Activity Towards Oxygen Reduction, Adv. Funct. Mater. 24(27) (2014) 4325-4336. https://doi.org/10.1002/adfm.201400161.

[29] Y. Yuan, S. Adimi, X. Guo, T. Thomas, Y. Zhu, H. Guo, G.S. Priyanga, P. Yoo, J. Wang, J. Chen, P. Liao, J.P. Attfield, M. Yang, A Surface-Oxide-Rich Activation Layer (SOAL) on Ni_2Mo_3N for a Rapid and Durable Oxygen Evolution Reaction, Angew. Chem. Int. Ed. 59(41) (2020) 18036-18041. https://doi.org/10.1002/anie.202008116.

[30] A.K. Tareen, G.S. Priyanga, S. Behara, T. Thomas, M. Yang, Mixed ternary transition metal nitrides: A comprehensive review of synthesis, electronic structure, and properties of engineering relevance, Prog. Solid. State Ch. 53 (2019) 1-26. https://doi.org/10.1016/j.progsolidstchem.2018.11.001.

[31] H. Shin, H.-i. Kim, D.Y. Chung, J.M. Yoo, S. Weon, W. Choi, Y.-E. Sung, Scaffold-Like Titanium Nitride Nanotubes with a Highly Conductive Porous Architecture as a Nanoparticle Catalyst Support for Oxygen Reduction, ACS Catal. 6(6) (2016) 3914-3920. https://doi.org/10.1021/acscatal.6b00384.

[32] W.F. Chen, J.T. Muckerman, E. Fujita, Recent developments in transition metal carbides and nitrides as hydrogen evolution electrocatalysts, Chem Commun (Camb) 49(79) (2013) 8896-909. https://doi.org/10.1039/c3cc44076a.

[33] D. Meng, S. Zhang, T. Thomas, R. Zhao, Y. Shi, F. Qu, M. Yang, Platinum decorated mesoporous titanium nitride for fuel-cell type methanol gas sensor, Sens. Actuators B Chem. 308 (2020). https://doi.org/10.1016/j.snb.2020.127713.

[34] M. Yang, R. Guarecuco, F.J. DiSalvo, Mesoporous Chromium Nitride as High Performance Catalyst Support for Methanol Electrooxidation, Chem. Mater. 25(9) (2013) 1783-1787. https://doi.org/10.1021/cm400304q.

[35] Z. Cui, R.G. Burns, F.J. DiSalvo, Mesoporous $Ti_{0.5}Nb_{0.5}N$ Ternary Nitride as a Novel Noncarbon Support for Oxygen Reduction Reaction in Acid and Alkaline Electrolytes, Chem. Mater. 25(19) (2013) 3782-3784. https://doi.org/10.1021/cm4027545.

[36] M. Yang, A.R. Van Wassen, R. Guarecuco, H.D. Abruna, F.J. DiSalvo, Nano-structured ternary niobium titanium nitrides as durable non-carbon supports for oxygen reduction reaction, Chem Commun (Camb) 49(92) (2013) 10853-5. https://doi.org/10.1039/c3cc45732j.

[37] C. Huang, S. Adimi, D. Liu, H. Guo, T. Thomas, J.P. Attfield, S. Ruan, F. Qu, M. Yang, Mesoporous titanium niobium nitrides supported Pt nanoparticles for highly selective and sensitive formaldehyde sensing, J. Mater. Chem. A (2021). https://doi.org/10.1039/d1ta02433g.

[38] H. Cui, G. Zhang, X. Zhang, J. Tang, Rh-doped $MoSe_2$ as a toxic gas scavenger: a first-principles study, Nanoscale Adv. 1(2) (2019) 772-780. https://doi.org/10.1039/c8na00233a.

456   [39] H. Cui, X. Zhang, G. Zhang, J. Tang, Pd-doped MoS_2 monolayer: A promising candidate for
457   DGA in transformer oil based on DFT method, Appl. Surf. Sci. 470 (2019) 1035-1042.
458   https://doi.org/10.1016/j.apsusc.2018.11.230.

459   [40] W. Ju, T. Li, X. Su, H. Li, X. Li, D. Ma, Au cluster adsorption on perfect and defective MoS_2
460   monolayers: structural and electronic properties, Phys. Chem. Chem. Phys. 19(31) (2017)
461   20735-20748. https://doi.org/10.1039/c7cp03062b.

462   [41] Y. Xiao, Z. Fu, G. Zhan, Z. Pan, C. Xiao, S. Wu, C. Chen, G. Hu, Z. Wei, Increasing Pt methanol
463   oxidation reaction activity and durability with a titanium molybdenum nitride catalyst support, J.
464   Power Sources 273 (2015) 33-40. https://doi.org/10.1016/j.jpowsour.2014.09.057.

465   [42] M. Roca-Ayats, G. García, J.L. Galante, M.A. Peña, M.V. Martínez-Huerta, TiC, TiCN, and TiN
466   Supported Pt Electrocatalysts for CO and Methanol Oxidation in Acidic and Alkaline Media, J. Phys.
467   Chem. C 117(40) (2013) 20769-20777. https://doi.org/10.1021/jp407260v.

468   [43] W. Liu, L. Xu, K. Sheng, X. Zhou, B. Dong, G. Lu, H. Song, A highly sensitive and
469   moisture-resistant gas sensor for diabetes diagnosis with $Pt@In_2O_3$ nanowires and a molecular sieve
470   for protection, NPG Asia Mater. 10(4) (2018) 293-308. https://doi.org/10.1038/s41427-018-0029-2.

471   [44] P.M. Bulemo, H.J. Cho, D.H. Kim, I.D. Kim, Facile Synthesis of Pt-Functionalized
472   Meso/Macroporous SnO_2 Hollow Spheres through in Situ Templating with SiO_2 for H_2S Sensors, ACS
473   Appl. Mater. Interfaces 10(21) (2018) 18183-18191. https://doi.org/10.1021/acsami.8b00901.

474   [45] S.-Y. Cho, H.-J. Koh, H.-W. Yoo, H.-T. Jung, Tunable Chemical Sensing Performance of Black
475   Phosphorus by Controlled Functionalization with Noble Metals, Chem. Mater. 29(17) (2017)
476   7197-7205. https://doi.org/10.1021/acs.chemmater.7b01353.

477   [46] R. Baron, J. Saffell, Amperometric Gas Sensors as a Low Cost Emerging Technology Platform
478   for Air Quality Monitoring Applications: A Review, ACS Sens. 2(11) (2017) 1553-1566.
479   https://doi.org/10.1021/acssensors.7b00620.

480   [47] R. Zhang, T. Zhou, L. Wang, T. Zhang, Metal-Organic Frameworks-Derived Hierarchical Co_3O_4
481   Structures as Efficient Sensing Materials for Acetone Detection, ACS Appl. Mater. Interfaces 10(11)
482   (2018) 9765-9773. https://doi.org/10.1021/acsami.7b17669.

483   [48] B. Song, D. Choi, Y. Xin, C.R. Bowers, H. Hagelin-Weaver, Ultra-Low Loading Pt/CeO_2
484   Catalysts: Ceria Facet Effect Affords Improved Pairwise Selectivity for Parahydrogen Enhanced NMR
485   Spectroscopy, Angew. Chem. Int. Ed. (2020). https://doi.org/10.1002/anie.202012469.

486   [49] X. Zheng, Y. Li, L. Zhang, L. Shen, Y. Xiao, Y. Zhang, C. Au, L. Jiang, Insight into the effect of
487   morphology on catalytic performance of porous CeO_2 nanocrystals for H_2S selective oxidation, Appl.
488   Catal. B 252 (2019) 98-110. https://doi.org/10.1016/j.apcatb.2019.04.014.

489   [50] T.-T. Zhang, Q.-L. Tang, M.-Y. Yao, C. Chen, X.-X. Duan, Q. Wang, X. Zhang, M.-L. Zhang, W.
490   Hu, Quantum chemical DFT study of molecular adsorption of H_2S on clean and chemically modified
491   Au(1 1 0) surfaces, Appl. Surf. Sci. 542 (2021). https://doi.org/10.1016/j.apsusc.2020.148595.

492   [51] Y. Liu, C. Song, Y. Wang, W. Cao, Y. Lei, Q. Feng, Z. Chen, S. Liang, L. Xu, L. Jiang, Rational
493   designed Co@N-doped carbon catalyst for high-efficient H_2S selective oxidation by regulating
494   electronic structures, Chem. Eng. J. 401 (2020). https://doi.org/10.1016/j.cej.2020.126038.
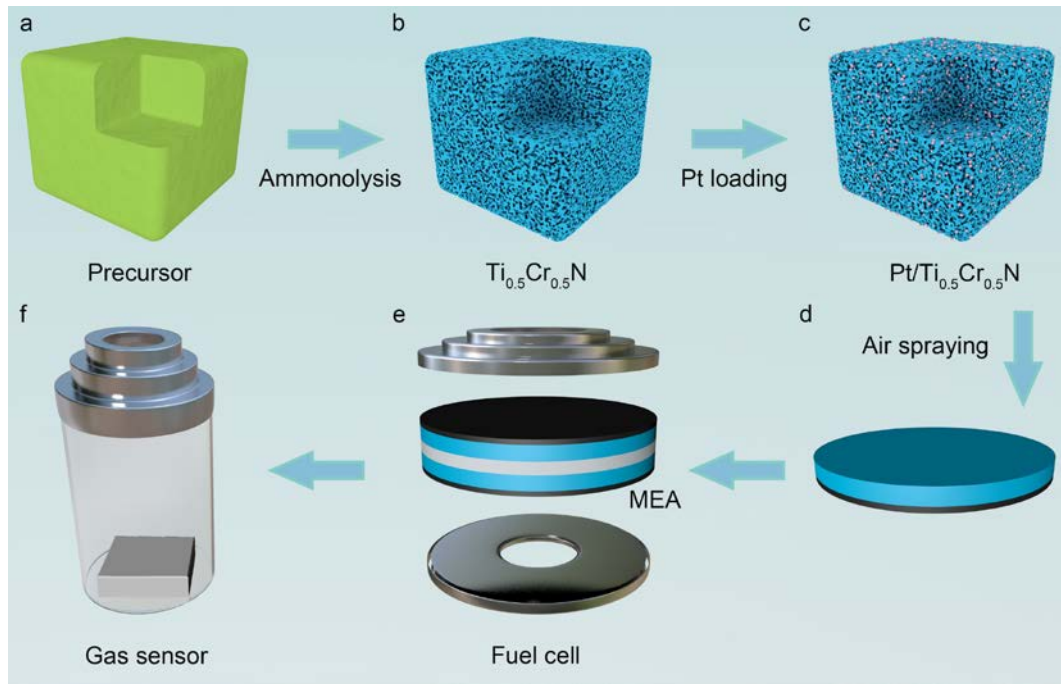
495   [52] W. Li, X. Yang, Y. Zhang, X. Hao, T. Liu, X. Liang, F. Liu, X. Yan, F. Liu, Y. Gao, J. Ma, G. Lu,

496   Amperometric H_2S sensor based on a Pt-Ni alloy electrode and a proton conducting membrane, Sens.
497   Actuators B Chem. 311 (2020). https://doi.org/10.1016/j.snb.2020.127900.

498

499

500

Fig. 1. Schematic illustration of fabrication process of fuel cell type gas sensor. a) Oxide precursor. b) Mesoporous $Ti_{0.5}Cr_{0.5}N$. c) Mesoporous $Ti_{0.5}Cr_{0.5}N$ as support of Pt NPs. d) Air spraying of catalyst ink on gas diffusion layer. e) The fuel cell consists of MEA and two metal electrodes. f) Schematic illustration of gas sensor.

505
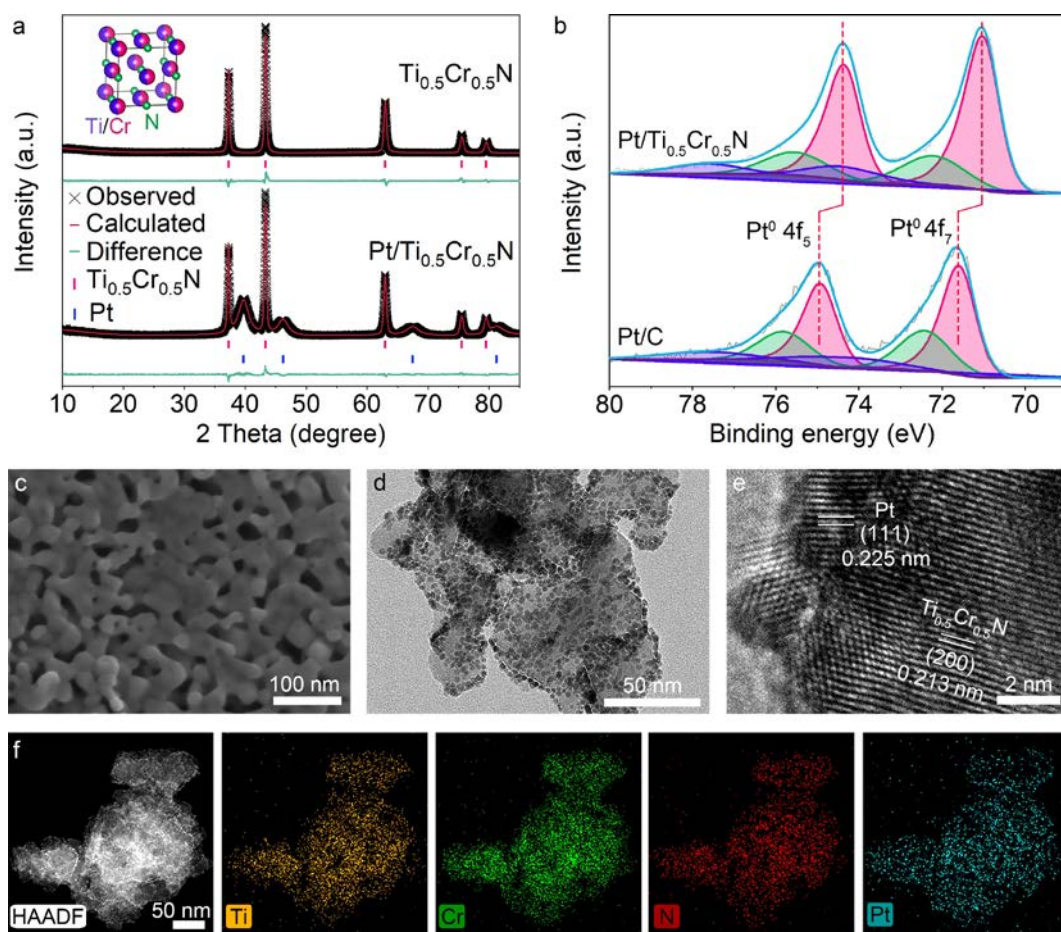
Fig. 2. a) Rietveld-refined powder XRD pattern of Pt/Ti$_{0.5}$Cr$_{0.5}$N and Ti$_{0.5}$Cr$_{0.5}$N. Space group; $Fm\bar{3}m$ for both Pt/Ti$_{0.5}$Cr$_{0.5}$N phases; Cell parameters; a = 4.1693(5) Å for Ti$_{0.5}$Cr$_{0.5}$N, a = 3.9215(5) Å for Pt; residuals wRp = 6.81%, R = 5.47%. b) XPS spectra of Pt/Ti$_{0.5}$Cr$_{0.5}$N and Pt/C in the Pt 4f region. c) SEM images of Ti$_{0.5}$Cr$_{0.5}$N and d) TEM images of Pt/Ti$_{0.5}$Cr$_{0.5}$N. e) High-resolution transmission electron microscopy (HRTEM) image of Pt/Ti$_{0.5}$Cr$_{0.5}$N. f) High-angle annular dark-field scanning TEM and EDX mapping images of Ti, Cr, N and Pt.
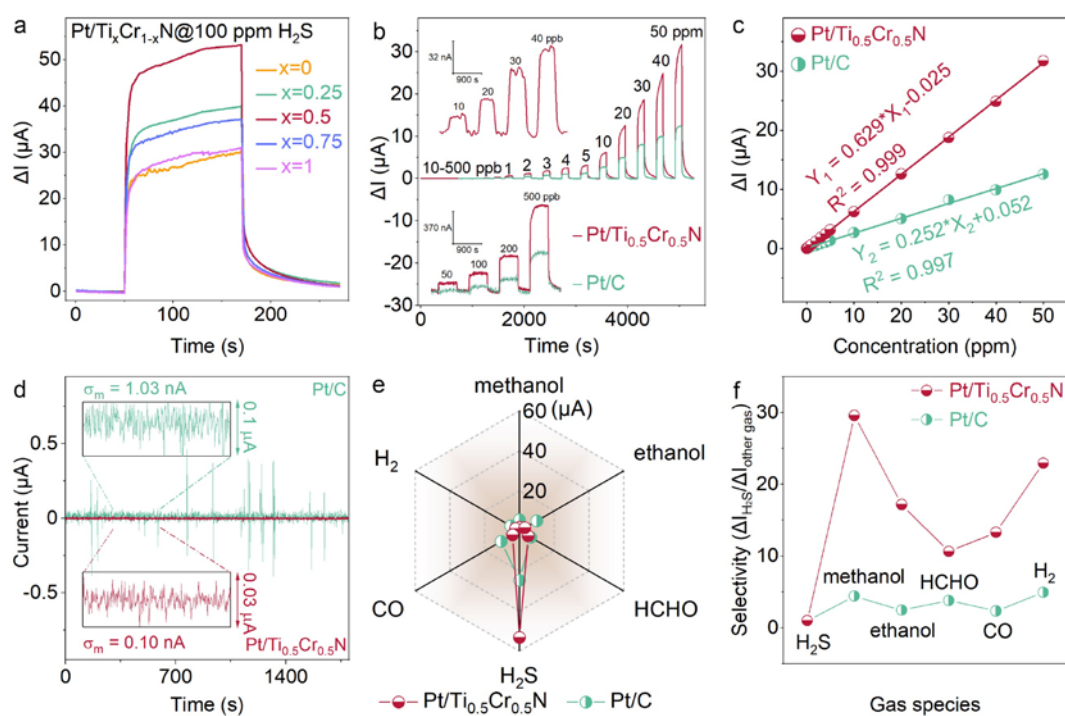
25

Fig. 3. a) The response transients of Pt/Ti$_x$Cr$_{1-x}$N sensor to 100 ppm (v) H$_2$S. b) Real-time responses and c) H$_2$S concentration-dependent response value of Pt/Ti$_{0.5}$Cr$_{0.5}$N and Pt/C-based sensor to 10 ppb (v)-50 ppm (v) H$_2$S. d) Current baseline of Pt/Ti$_{0.5}$Cr$_{0.5}$N and Pt/C sensor in air. The insets show zoomed-in regions spanning 300 s. e) Selectivity and f) selectivity improvements of Pt/Ti$_{0.5}$Cr$_{0.5}$N and Pt/C sensor toward various analyte gases.

521
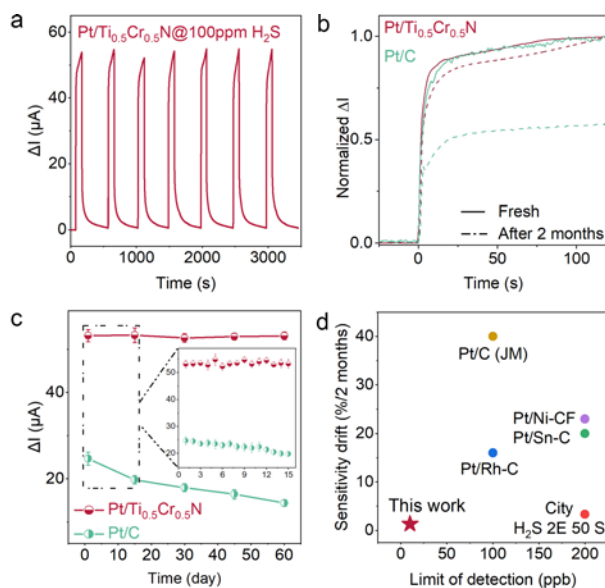
Fig. 4. Stability evaluation: a) 7-cycle dynamic sensing response of Pt/Ti$_{0.5}$Cr$_{0.5}$N sensor to 100 ppm
(v) H$_2$S. b) Normalized real-time responses of Pt/Ti$_{0.5}$Cr$_{0.5}$N and Pt/C-based sensor to 100 ppm (v)
H$_2$S at different aging states. c) Long-term stability of Pt/Ti$_{0.5}$Cr$_{0.5}$N and Pt/C sensor. d) Comparison
of selected fuel cell type sensors and commercial 2-electrode H$_2$S sensor with Pt/Ti$_{0.5}$Cr$_{0.5}$N.[24, 25,
52]

527
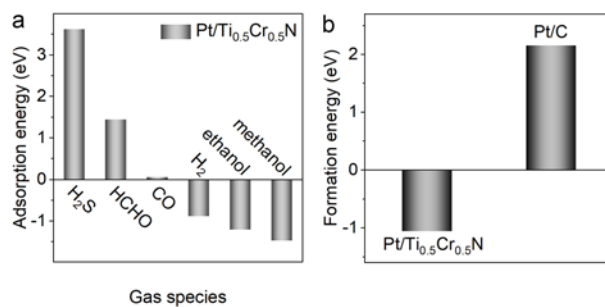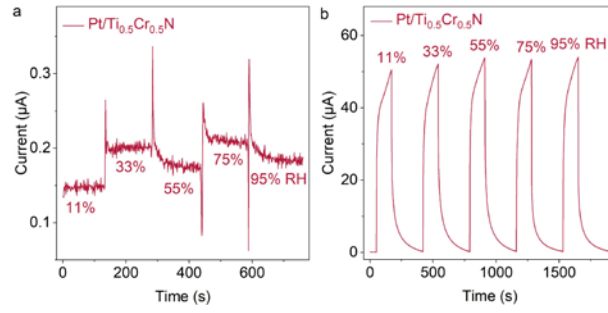
Fig. 5. a) Adsorption energy of various gas molecule on Pt(111)/Ti$_{0.5}$Cr$_{0.5}$N. b) Formation energy of Pt combined with Ti$_{0.5}$Cr$_{0.5}$N and C support.

532

Fig. 6. The influence of relative humidity (RH) on the gas sensing performance of the sensor. a)
baseline current and b) transient response under different RH.